Available online at www.sciencedirect.com
ScienceDirect
Journal of Computational Physics 227 (2008) 3141–3158
JOURNAL OF COMPUTATIONAL PHYSICS
www.elsevier.com/locate/jcp

Flux limiting embedded boundary technique for electromagnetic FDTD

M.T. Bettencourt *,[1]

Air Force Research Laboratory, Kirtland Air Force Base, Albuquerque, NM 87117, United States

Received 27 February 2007; received in revised form 8 November 2007; accepted 15 November 2007
Available online 15 December 2007

Abstract

A general approach for incorporating embedded boundaries into an electromagnetic finite difference time domain (FDTD) code is presented. This algorithm is shown to satisfy Gauss's law and enforces no magnetic monopoles while maintaining a globally second-order result (first-order at physical boundaries), with no added time-step restriction. Theoretically predicted superior results are shown with an 11% time-step reduction from the Courant stability limit. This is achieved through a physics-based flux limiting scheme near physical boundaries. Stability, local truncation error and energy conservation analysis are also provided.
Published by Elsevier Inc.

Keywords: Electromagnetic; EM; Finite difference time domain; FDTD; Conformal boundaries; Embedded boundaries; Flux limiting

1. Introduction

The finite difference time domain (FDTD) technique for solving Maxwell's equations has been a very powerful tool in the simulation of electromagnetic phenomena since its introduction by Yee [1]. Computational efficiency, ease of implementation, second-order accuracy (in the absence of physical boundaries) and energy conservation are among the method's many positive qualities. Furthermore, this scheme can be extended to include plasmas with particle-in-cell (PIC) techniques. However, a key weakness of the scheme is the low order boundary representation of physical geometry which can drop the global accuracy of the method to first-order for many physical geometries.

There have been many attempts to mitigate the errors caused by stair-cased boundaries in FDTD simulations through both the use of unstructured grids and solving Maxwell's equations on cut cells embedded in an otherwise structured grid. While fully unstructured grids are the mainstay in frequency domain codes, they are making inroads into time domain applications both for finite vols [2], finite element methods [3] and for spectral element codes [4]. These methods offer the flexibility of unstructured gridding, however they are more

* Tel.: +1 505 853 4320; fax: +1 505 846 0417.
E-mail address: icepic@kirtland.af.mil
[1] Research supported by a Grant from the Air Force Office of Sponsored Research (AFOSR) Contract number F2960100D00550031.

0021-9991/$ - see front matter Published by Elsevier Inc.
doi:10.1016/j.jcp.2007.11.043

complicated to implement, can suffer from long-time instabilities [5] and the incorporation of particles into these simulation techniques [6] is an unresolved area of research.

Several modifications to the standard FDTD algorithm have been proposed which maintain the inherit simplicity in the bulk of the domain and require special attention only adjacent to physical boundaries. The first of these is the scheme of Dey and Mittra [7], where the time-step is reduced and fractional cells of a sufficient size are handled through the standard algorithm. The work by Yu and Mittra [8] removed the time-step restriction required by [7], however, as shown in [9], the Yu–Mittra algorithm has a lower level of accuracy than the Dey–Mittra scheme. Benkler et al. [9] proposed a modified scheme similar to Yu–Mittra which simplified the computation and incorporated a reduced time-step to improve accuracy through improved accounting of the magnetic field area. The Benkler scheme shows improved accuracy over the Dey–Mittra and Yu–Mittra schemes listed above. Contour methods originally proposed by Jurgens et al. [10] modify the standard FDTD by using the integral forms of Maxwell's equations near physical boundaries. These methods, like the Dey–Mittra scheme, require a reduction in time-step to maintain stability.

In addition to the schemes listed above there exist a class of schemes known as area borrowing algorithms [11]. These algorithms enlarge cell volumes over a threshold by moving volume from a full cell to a partial cell in order to stabilize small cells. This class of methods trade the numerical complexity of updating partial cells below the stability limit with the geometric complexity of creating a set of sufficiently large cells around a physical boundary, which can be intractable in three-dimensions.

This article presents a new procedure for representing conformal boundaries within an FDTD code. This work is inspired by the research of Berger and Leveque [12] and Colella et al. [13] where the fluxes into a computational cell are redistributed based on geometric considerations. Unlike the schemes listed above, individual fluxes are limited on a face-by-face basis instead of a cell based flux redistribution.

A brief review of the traditional FDTD method proposed by Yee [1] follows. Section 3 presents a detailed one-dimensional analysis the stability, accuracy and energy conservation properties of the proposed method. Section4 extends the one-dimensional algorithm to multiple dimensions. Results showing second-order accuracy are presented for simple cavity problems and qualitative results are given for more complex geometries.

2. Standard finite difference time domain

We start with Maxwell's equations shown in differential form,

$$\frac{\partial \mathbf{B}}{\partial} = -\nabla \times \mathbf{E} \tag{1a}$$

$$\frac{\partial \mathbf{D}}{\partial} = \nabla \times \mathbf{H} - \mathbf{J} \tag{1b}$$

$$\nabla \cdot \mathbf{B} = 0 \tag{1c}$$

$$\nabla \cdot \mathbf{D} = \rho \tag{1d}$$

$$\mathbf{B} = \mu \mathbf{H} \tag{1e}$$

$$\mathbf{D} = \epsilon \mathbf{E} \tag{1f}$$

where $\mathbf{E}$ and $\mathbf{H}$ are the electric and magnetic fields respectively, $\mathbf{D}$ and $\mathbf{B}$ are the electric and magnetic flux densities respectively and μ, ϵ, ρ and $\mathbf{J}$ are the material permeability, permittivity, charge and current densities. The speed of light, $c = \frac{1}{\sqrt{\mu\epsilon}}$, is defined for convenience. Values written as $\mathbf{V}$ are assumed to be vectors of the form $(V_\iota, V_\kappa, V_\jmath)$.

The standard finite difference time domain (FDTD) solves these equations in a leap-frog method on a staggered grid as shown in Fig. 1. This leads to the standard update equation:

$$B^{n+\frac{1}{2}}_{\iota;i+\frac{1}{2},j+\frac{1}{2},k} = B^{n-\frac{1}{2}}_{\iota;i+\frac{1}{2},j+\frac{1}{2},k} - \frac{\Delta}{\Delta}\left(E^n_{\kappa;i+1,j+\frac{1}{2},k} - E^n_{\kappa;i,j+\frac{1}{2},k}\right) + \frac{\Delta}{\Delta\kappa}\left(E^n_{\jmath;i+\frac{1}{2},j+1,k} - E^n_{\jmath;i+\frac{1}{2},j,k}\right) \tag{2}$$

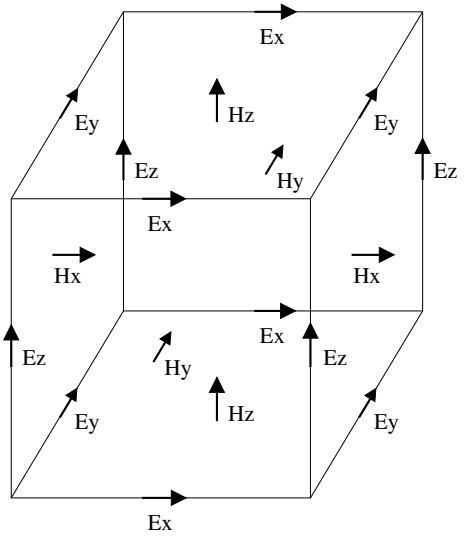

Fig. 1. Three-dimensional Yee mesh.

$$E^{n+1}_{\kappa;i,j+\frac{1}{2},k} = E^{n}_{\kappa;i,j+\frac{1}{2},k} - \frac{\Delta}{\epsilon_{i,j+\frac{1}{2},k}} J_{\kappa;i,j+\frac{1}{2},k} - \frac{\Delta}{\epsilon_{i,j+\frac{1}{2},k}\Delta}\left(\frac{1}{\mu_{i+\frac{1}{2},j+\frac{1}{2},k}} B^{n+\frac{1}{2}}_{;i+\frac{1}{2},j+\frac{1}{2},k} - \frac{1}{\mu_{i-\frac{1}{2},j+\frac{1}{2},k}} B^{n+\frac{1}{2}}_{;i-\frac{1}{2},j+\frac{1}{2},k}\right)$$
$$+ \frac{\Delta}{\epsilon_{i,j+\frac{1}{2},k}\Delta}\left(\frac{1}{\mu_{i,j+\frac{1}{2},k+\frac{1}{2}}} B^{n+\frac{1}{2}}_{;i,j+\frac{1}{2},k+\frac{1}{2}} - \frac{1}{\mu_{i,j+\frac{1}{2},k-\frac{1}{2}}} B^{n+\frac{1}{2}}_{;i,j+\frac{1}{2},k-\frac{1}{2}}\right) \tag{3}$$

and similar equations for the remaining two **B** and **E** components. These equations are stable if

$$\Delta \leqslant \frac{1}{c\sqrt{\frac{1}{\Delta^2} + \frac{1}{\Delta\kappa^2} + \frac{1}{\Delta^2}}} \tag{4}$$

This formulation has the property of discretely satisfying the divergence constraint. Furthermore, by applying the Poynting theorem to the discrete equations it can be shown that this algorithm conserves energy in the discrete sense if one neglects temporal interpolation errors which do not accumulate in time.

The algorithm described above assumes that all cells are the same size and physical geometry is approximated with a stair-cased representation. The remainder of this paper documents a procedure where physical geometry can be represented with a piecewise linear boundary while maintaining many of the properties of the original scheme. Furthermore, the remainder of the document will assume an isotropic grid with normalized spatial parameters and no source terms as follows:

$$\begin{aligned} &\Delta \ = \Delta\kappa = \Delta \ = h \\ &\mu = \mu_0 \quad \epsilon = \epsilon_0 \quad c = \sqrt{\frac{1}{\mu_0\epsilon_0}} \\ &\mathbf{J} = \rho = 0 \end{aligned} \tag{5}$$

3. One-dimensional theory

The one-dimensional discrete form of Yee's method is shown in (6a) and (6b). Integer cell indices refer to the edge of grids (location of **E**) and fractional indices refer to cell centered values (location of **B**) as shown in Fig. 2.

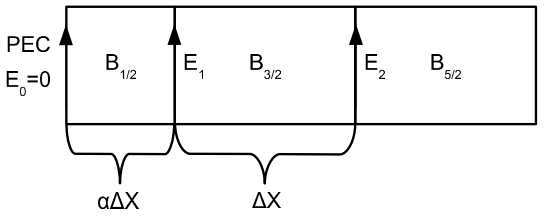

Fig. 2. Representation of grid centering and dimensional parameters. E values live on the cell edges where B values live in the centers of the cells, both for the full and fractional cells.

$$B_{i+\frac{1}{2}}^{n+\frac{1}{2}} = B_{i+\frac{1}{2}}^{n-\frac{1}{2}} - \frac{\Delta}{h}\left(E_{i+1}^{n} - E_{i}^{n}\right) \tag{6a}$$

$$E_{i}^{n+1} = E_{i}^{n} - c^2\frac{\Delta}{h}\left(B_{i+\frac{1}{2}}^{n+\frac{1}{2}} - B_{i-\frac{1}{2}}^{n+\frac{1}{2}}\right) \tag{6b}$$

The well-known stability limit for these update equations is based on the Courant Friedrichs Levy (CFL) condition, $\gamma = \frac{c\Delta}{h} < 1$, assuming a uniform mesh spacing. It turns out one can stably reduce the mesh spacing adjacent to a perfectly electrically conducting (PEC) boundary to roughly 71% ($\alpha = \frac{1}{\sqrt{2}}$ in Fig. 2, where α is the fractional cell percentage) without incurring a time-step penalty. Starting with the one-dimensional update equations for the fractional cell:

$$B_{\frac{1}{2}}^{n+\frac{1}{2}} = B_{\frac{1}{2}}^{n-\frac{1}{2}} - \frac{\Delta}{\alpha h}E_{1}^{n} \tag{7a}$$

$$E_{1}^{n+1} = E_{1}^{n} - c^2\frac{2\Delta}{h(1+\alpha)}\left(B_{\frac{3}{2}}^{n+\frac{1}{2}} - B_{\frac{1}{2}}^{n+\frac{1}{2}}\right) \tag{7b}$$

which can be combined into two equivalent second-order forms:

$$\frac{B_{\frac{1}{2}}^{n+\frac{3}{2}} - 2B_{\frac{1}{2}}^{n+\frac{1}{2}} + B_{\frac{1}{2}}^{n-\frac{1}{2}}}{\Delta^2} = c^2\frac{2}{\alpha(\alpha+1)}\frac{B_{\frac{3}{2}}^{n+\frac{1}{2}} - B_{\frac{1}{2}}^{n+\frac{1}{2}}}{h^2} \tag{8a}$$

$$\frac{E_{1}^{n+1} - 2E_{1}^{n} + E_{1}^{n-1}}{\Delta^2} = c^2\frac{2}{\alpha(\alpha+1)}\frac{\alpha E_{2}^{n} - (1+\alpha)E_{1}^{n}}{h^2} \tag{8b}$$

Following the procedure illustrated in Taflove [14] and using the basis functions $B = B_0 e^{-i(\omega - k)}$ and $E = E_0 e^{-i(\omega - k)}$ yields the following stability criteria:

$$-1 < 1 + \gamma^2\frac{1}{\alpha(\alpha+1)}\left(e^{ikh} - 1\right) < 1 \tag{9a}$$

$$-1 < 1 + \gamma^2\frac{1}{\alpha(\alpha+1)}\left(\alpha e^{ikh} - (1+\alpha)\right) < 1 \tag{9b}$$

Eqs. (9a) and (9b) represent an upper bound on the stability limit and help to provide insight into the stability of the numerics. However, due to the non-constant stencil one must use an eigenvalue analysis to determine the true stability limit. It can be seen from (9a) and (9b) that the $kh = \pi$, or checker-board, mode is the most critical mode with respect to stability. Restricting the analysis to this mode allows one to perform an eigenvalue analysis with a partial matrix. For the checker-board mode, each full cell has the same magnitude of **B**, but an opposite sign. This is equivalent to a Neumann boundary condition for **B**, and thus making $B_{\frac{5}{2}} = -B_{\frac{3}{2}}$. Therefore, one only needs to represent the cells directly affected by the cut cell with the remaining cells being folded into a boundary condition in the matrix. This is expressed in matrix form below:

$$\begin{bmatrix} -\frac{2\gamma^2}{\alpha(\alpha+1)} & \frac{2\gamma^2}{\alpha(\alpha+1)} & 0 \\ \frac{2\gamma^2}{\alpha+1} & -\frac{\gamma^2(\alpha+3)}{\alpha+1} & \gamma^2 \\ 0 & \gamma^2 & -3\gamma^2 \end{bmatrix} - \lambda I = 0 \tag{10}$$

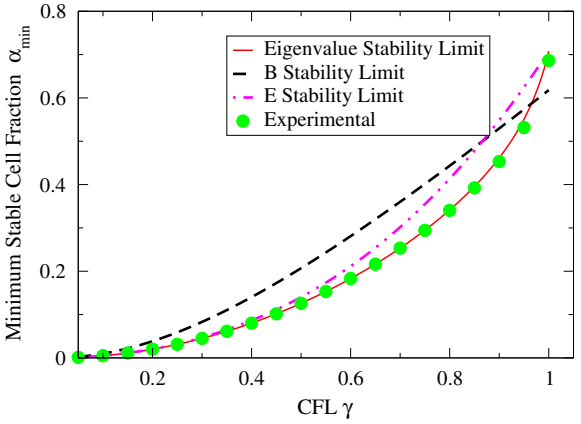

Fig. 3. Cell fraction as a function of CFL condition.

Solving for the eigenvalues and setting the smallest one to the stability limit [14], $\lambda_{\min} = -4$, yields the following expression for α_1 (the lowest alpha which can be stably advanced without any modification) as a function of γ.

$$\alpha_1 = \frac{-8 + 12\gamma^2 - 4\gamma^4 + \sqrt{2}\sqrt{\gamma^{10} - 8\gamma^8 + 32\gamma^6 - 24\gamma^4 - 32\gamma^2 + 32}}{2(\gamma^4 - 8\gamma^2 + 8)} \tag{11}$$

Fig. 3 is the minimum cell fraction plotted against γ as predicted by (11). In addition to the eigenvalue solutions, the predicted stability curves for (9a) and (9b) are also plotted. Results from an experimental one-dimensional code are also plotted showing excellent agreement to the eigenvalue theory.

Previous cut-cell methods have achieved stability by reducing the time-step. This allows for the representation of more of the physical geometry, and exchanges computational effort for accuracy, a technique which offers limited improvement. By lowering the time-step, one not only requires more time steps to be computed, one also decreases the accuracy of the method due to the increase in dispersion of the method, [14]. In essence, one trades geometric errors for dispersive errors. The proposed flux limiting scheme improves on existing cut-cell schemes by achieving the required stability for all cut cells without imposing a reduced time-step and increasing dispersion error.

To help understand the flux limiting stabilizing algorithm, it is convenient to view the update in a conservative form:

$$\frac{\partial \mathbf{B}}{\partial} + \nabla \cdot \mathbf{F}_B = 0 \tag{12}$$

where $\mathbf{F}_B$ is the flux of $\mathbf{B}$ entering a volume. In the case of one-dimensional Maxwell's equations, the flux is just E_κ. In three-dimensions the flux is

$$\mathbf{F}_B = \begin{bmatrix} 0 & -E & E_\kappa \\ E & 0 & -E \\ -E_\kappa & E & 0 \end{bmatrix} \tag{13}$$

To stabilize the scheme listed above across all α's, one can limit the fluxes entering a fractional cell. It is sufficient to linearly decrease the flux of $\mathbf{B}$ into a cut cell from the minimum α where the standard scheme goes unstable, α_1 as shown in (14).

$$F_B = \begin{cases} E_\kappa & \alpha > \alpha_1 \\ E_\kappa \frac{\alpha}{\alpha_1} & \alpha <= \alpha_1 \end{cases} \tag{14}$$

To show this, one modifies (10) to take into account the effect of the limited flux, $\mathbf{F}_B$.

$$\begin{bmatrix} -\frac{2\gamma^2}{\alpha_l(\alpha+1)} & \frac{2\gamma^2}{\alpha_l(\alpha+1)} & 0 \\ \frac{2\gamma^2\alpha}{\alpha_l(\alpha+1)} & -\frac{\gamma^2(2\alpha+(\alpha+1)\alpha_l)}{\alpha_l(\alpha+1)} & \gamma^2 \\ 0 & \gamma^2 & -3\gamma^2 \end{bmatrix} - \lambda I = 0 \tag{15}$$

Here α_l is the solution to the eigenvalue stability equation (11). This yields a modified stability diagram as shown in Fig. 4, where the smallest eigenvalue is plotted against α for various γ's. Since all values of the eigenvalues are in the desired range, $[-4, 0]$, the scheme is determined to be stable across all α's and γ's less than unity.

The prior analysis assumed a semi-infinite domain extending from a cut cell. If this is reduced to the limiting case, a geometry with only two cut cells, an eigenvalue analysis can be performed. This results in two eigenvalues, 0 and $\frac{-2\gamma^2}{\alpha_L\alpha_R}$, where α_L and α_R are the left and right cell fractions, respectively. This problem can be stabilized by limiting the flux of **B** as follows:

$$\mathbf{F}_B = \min\left(\frac{2\alpha_L\alpha_R}{\gamma^2}, 1\right)\mathbf{E} \tag{16}$$

This scheme stabilizes one-dimensional FDTD algorithms so that they can handle cut cells. However, this is only beneficial if it improves the quality of the solution and, ideally, maintains second-order convergence in at least the L_1 norm, where the norms are defined as

$$\begin{aligned} L_\infty &= \max(|B_{\text{exact}} - B_i^n|) \\ L_1 &= \frac{\sum_{i=0}^{NX}(|B_{\text{exact}} - B_i^n|\alpha_i\Delta\ )}{\sum_{i=0}^{NX}\alpha_i\Delta} \\ L_2 &= \sqrt{\frac{\sum_{i=0}^{NX}((B_{\text{exact}} - B_i^n)^2\alpha_i\Delta\ )}{\sum_{i=0}^{NX}\alpha_i\Delta}}. \end{aligned} \tag{17}$$

One can compute the theoretical order of convergence using a modified equation analysis. The truncation error τ is the difference between an exact solution for **B** and the discrete update of that exact solution for one time-step, normalized by the length of the time-step.

$$\tau = \frac{B_{\text{exact}}^{n+\frac{3}{2}}\left(\frac{\alpha h}{2}\right) - B_{\frac{1}{2}}^{n+\frac{3}{2}}}{B_{\text{exact}}^{n+\frac{3}{2}}\Delta} \tag{18}$$

One can calculate the discrete update for $B_{\frac{1}{2}}^{n+\frac{3}{2}}$ as follows:

$$B_{\frac{1}{2}}^{n+\frac{3}{2}} = B_{\frac{1}{2}}^{n+\frac{1}{2}} - \frac{\alpha\Delta}{\alpha_{0,l}h}(E_1^{n+1}) \tag{19a}$$

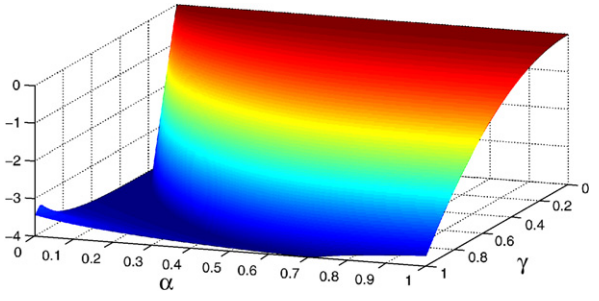

Fig. 4. Flux limited one-dimensional stability plot showing the smallest eigenvalue for the modified Eq. (15). Eigenvalues between 0 and −4 are stable.

$$E_1^{n+1} = E_1^n - c^2 \frac{2\Delta}{(1+\alpha)h}\left(B_{\frac{3}{2}}^{n+\frac{1}{2}} - B_{\frac{1}{2}}^{n+\frac{1}{2}}\right) \tag{19b}$$

$$B_{\frac{1}{2}}^{n+\frac{3}{2}} = 2B_{\frac{1}{2}}^{n+\frac{1}{2}} - B_{\frac{1}{2}}^{n-\frac{1}{2}} + c^2 \frac{2\alpha\Delta^2}{\alpha_{0,1}(1+\alpha)h^2}\left(B_{\frac{3}{2}}^{n+\frac{1}{2}} - B_{\frac{1}{2}}^{n+\frac{1}{2}}\right) \tag{19c}$$

$$\alpha_{0,1} = \begin{cases} \alpha & \alpha > \alpha_1 \\ \alpha_1 & \alpha \leqslant \alpha_1 \end{cases} \tag{19d}$$

Assuming one knows all values for B at times less than $n+\frac{3}{2}$ one can insert (19c) into (18) to compute the truncation error, τ. Using the exact solution:

$$B(\ ,\ ) = e^{i(\omega\ )}\cos(k\ ) \tag{20}$$

yields

$$\tau = \frac{e^{i\omega\Delta} - 2 + e^{-i\omega\Delta} - c^2 \frac{2\alpha\Delta^2}{\alpha_{0,1}(1+\alpha)h^2}\left(\frac{\cos(k\frac{2\alpha+1}{2}h)}{\cos\left(k\frac{\alpha h}{2}\right)} - 1\right)}{\Delta} \tag{21}$$

Substituting in sines and cosines for the complex exponentials yields

$$\tau = \frac{-4\sin^2\left(\frac{\omega\Delta}{2}\right) - c^2 \frac{2\alpha\Delta^2}{\alpha_{0,1}(1+\alpha)h^2}\left(\frac{\cos\left(k\frac{2\alpha+1}{2}h\right)}{\cos\left(k\frac{\alpha h}{2}\right)} - 1\right)}{\Delta} \tag{22}$$

Assuming that you are adequately resolved, therefore $kh \ll 1$ and $\omega\Delta \ll 1$ one can expand the sine and cosine functions yielding

$$\tau = \frac{-(\omega\Delta\ )^2 + c^2 \frac{2\alpha\Delta^2}{\alpha_{0,1}(1+\alpha)h^2}\left(\frac{(3\alpha+1)(\alpha+1)}{8}(kh)^2\right) + O(h^2, \Delta^3)}{\Delta} \tag{23}$$

Noting that $\frac{\omega}{k} = c$ and simplifying results in

$$\tau = -\omega^2\Delta\left(1 - \frac{\alpha(3\alpha+1)}{4\alpha_{0,1}}\right) + O(h^2, \Delta^2) \tag{24}$$

The standard argument [15] is that if one maintains first-order accuracy on a domain one-dimension lower than the problem domain (assuming that the lower order domain is not along a characteristic path), the global solution will be first-order accurate in the L_∞ norm, second in the L_1 norm and somewhere in the middle for the L_2 norm. For cell fractions between zero and unity, $0 \leqslant \alpha < 1$, the method converges at a rate of $O(\Delta\ )$, thus satisfying the criteria above for a global second-order solution. It is important to note, that for $\alpha \to 1$ the first-order term drops out and with $\gamma \to 1$ the method becomes exact.

The L_∞ norm of the truncation error was verified for the one-dimensional problem of length l with the initial condition of $B(\ ,0) = \cos\left(2\pi\frac{}{l}\right)$. The results were plotted for several values of α and refinement and are shown in Fig. 5. These results show that the truncation error follows the first-order line very closely and thus satisfies the criteria for second-order convergence.

A comparison of the one-dimensional cut cell algorithm with a standard stair-stepped boundary method for a Gaussian pulse over a simulation time of $\frac{5L}{c}$ and a full range of cell fractions with a $\gamma = 0.9999$ and a $\alpha_1 = 0.707$ reveals that the cut cell algorithm is superior for all α's as shown in Fig. 6.

A refinement study was performed for the one-dimensional test code, in which the physical problem size was held fixed while more cells were added to the problem domain, thus reducing the effect of the stair-cased boundary. Fig. 7 shows that the cut-cell solution closely follows the second-order reference line, whereas the stair-cased solution varies widely depending on how the problem edge is aligned with the stair-cased edge, but is approximately first-order. The L_∞ norm shows better than expected convergence, this is due to the combined effect of both increasing the resolution and increasing α as one refines the problem, thus reducing the effect of flux limiting in the cut cell.

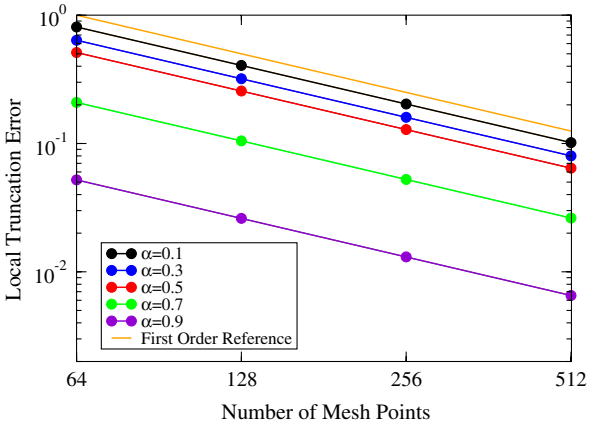

Fig. 5. L_∞ truncation error for a one-dimensional cosine wave along a line after one time-step with a γ of 0.9999.

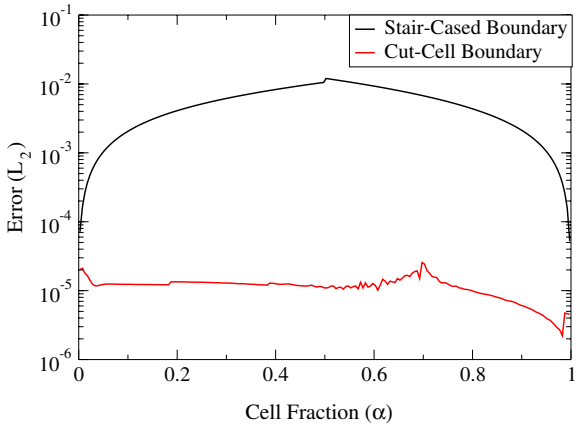

Fig. 6. L_2 error for a one-dimensional Gaussian pulse along a line after five oscillation periods as a function of cell fraction for both standard Yee and cut cells. CFL = 0.9999, $\alpha_1 = 0.707$, number of cells = 64.

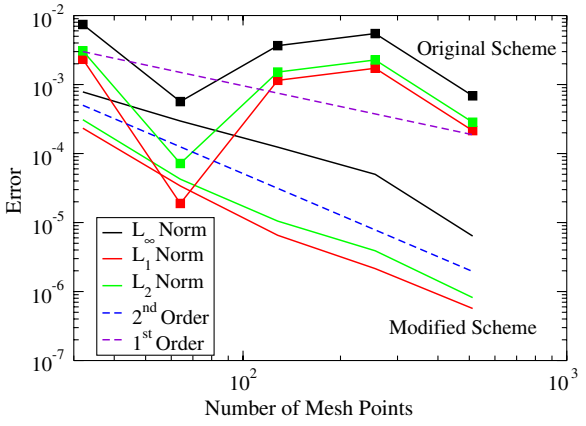

Fig. 7. Error for a one-dimensional Gaussian pulse along a line after ten oscillation periods as a function of level of refinement for both standard Yee (lines with square symbols) and cut cells (plain lines).

The Poynting theorem (25) states the principle of conservation of energy (W) for an electromagnetic field in the absence of currents.

$$\frac{\partial W}{\partial} = \nabla \cdot \mathbf{S} + \mathbf{E} \cdot \frac{\partial \mathbf{D}}{\partial} + \mathbf{H} \cdot \frac{\partial \mathbf{B}}{\partial} = 0 \tag{25}$$
$$\mathbf{S} = \mathbf{E} \times \mathbf{H}$$

One advantage of the original Yee scheme is that it conserves energy; while the modified scheme possesses a lower error, it no longer conserves energy. The discrete forms of the time derivatives are inserted into (25) and the equation is integrated across the two cells adjacent to the wall yielding

$$\frac{\partial W}{\partial} = \frac{\alpha - \alpha_{0,1}}{\alpha_{0,1}} E_1 \left(B_{\frac{3}{2}} - B_{\frac{1}{2}} \right) \tag{26}$$

It is important to note in (26) that if limiting is turned off ($\alpha_{0,1} = \alpha$) that this reverts to energy being conserved. Furthermore, while this scheme is not strictly energy conserving, any wave coming into a fractional cell will be reflected with the same sign of **B**, but an opposite sign on **E**, and therefore, the time averaged energy loss/gain is zero due to cancellation. This is shown in two-dimensions in the next section.

4. Multi-dimensional analysis and results

One-dimensional analysis showed the proposed scheme for approximating cut cells in FDTD codes was stable and converged globally second-order while not requiring any time-step restrictions. In this section, the scheme and analysis will be extended to two-dimensions.

4.1. Two-dimensional analysis

The analysis in this section mirrors that of the previous section and the notation follows that outlined in Fig. 8. Here, α , α_κ are the length fraction for the x and y edges. $A_{i,j}$ is the area of the cell spanning from $(\ _i, \kappa_j) \rightarrow (\ _{i+1}, \kappa_{j+1})$ which is not covered in PEC.

The update equations in the fractional cell are as follows:

$$B^{n+\frac{3}{2}}_{i+\frac{1}{2},j+\frac{1}{2}} = B^{n+\frac{1}{2}}_{i+\frac{1}{2},j+\frac{1}{2}} + \frac{h\Delta}{A_{i,j}} \left(\alpha\ E^{n+1}_{;i+\frac{1}{2},j+1} - \alpha_\kappa E^{n+1}_{\kappa;i+1,j+\frac{1}{2}} \right) \tag{27a}$$

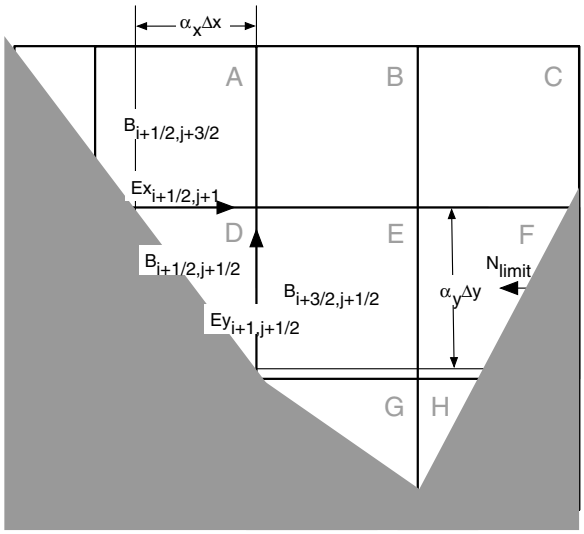

Fig. 8. Representation of grid centering and dimensional parameters for a cut two-dimensional grid.

$$E^{n+1}_{;i+\frac{1}{2},j+1} = E^{n}_{,i+\frac{1}{2},j+1} + c^2 \frac{2\alpha\ h\Delta}{(A_{i,j} + A_{i,j+1})}\left(B^{n+\frac{1}{2}}_{i+\frac{1}{2},j+\frac{3}{2}} - B^{n+\frac{1}{2}}_{i+\frac{1}{2},j+\frac{1}{2}}\right) \tag{27b}$$

$$E^{n+1}_{\kappa;i+1,j+\frac{1}{2}} = E^{n}_{\kappa,i+1,j+\frac{1}{2}} - c^2 \frac{2\alpha_\kappa h\Delta}{(A_{i,j} + A_{i+1,j})}\left(B^{n+\frac{1}{2}}_{i+\frac{3}{2},j+\frac{1}{2}} - B^{n+\frac{1}{2}}_{i+\frac{1}{2},j+\frac{1}{2}}\right) \tag{27c}$$

Substituting (27b) and (27c) into (27a) results in a second-order update equation for **B**:

$$B^{n+\frac{3}{2}}_{i+\frac{1}{2},j+\frac{1}{2}} - 2B^{n+\frac{1}{2}}_{i+\frac{1}{2},j+\frac{1}{2}} + B^{n-\frac{1}{2}}_{i+\frac{1}{2},j+\frac{1}{2}} = c^2 \frac{4\alpha\ \Delta^{\ 2}}{\alpha_\kappa(A_{i,j} + A_{i,j+1})}\left(B^{n+\frac{1}{2}}_{i+\frac{1}{2},j+\frac{3}{2}} - B^{n+\frac{1}{2}}_{i+\frac{1}{2},j+\frac{1}{2}}\right) + c^2 \frac{4\alpha_\kappa\Delta^{\ 2}}{\alpha\ (A_{i,j} + A_{i+1,j})}\left(B^{n+\frac{1}{2}}_{i+\frac{3}{2},j+\frac{1}{2}} - B^{n+\frac{1}{2}}_{i+\frac{1}{2},j+\frac{1}{2}}\right) \tag{28}$$

From (28), one sees that the stability of the update depends on the neighboring areas. Furthermore, the smaller the area, the more strict the stability criteria, i.e., the cell with smallest area has the most strict stability criteria when compared to a neighboring cell. In Fig. 8 cell D would have a stricter stability criteria than either cell A or E. If, for the time being, we neglect regions where the surface normal changes sign in the direction of differencing (the X direction in Fig. 8 for cells G and H), we can assume that the neighboring area is at least $\alpha\ h^2$ for the upper cell and $\alpha_\kappa h^2$ for the cell to the right of the cell of interest. Using the standard definition for the CFL condition in two-dimensions, $\gamma = \frac{c\Delta}{\sqrt{2}h}$, yields the following update equation:

$$B^{n+\frac{3}{2}}_{i+\frac{1}{2},j+\frac{1}{2}} - 2B^{n+\frac{1}{2}}_{i+\frac{1}{2},j+\frac{1}{2}} + B^{n-\frac{1}{2}}_{i+\frac{1}{2},j+\frac{1}{2}} = +\frac{4\gamma^2}{\alpha_\kappa(\alpha_\kappa + 2)}\left(B^{n+\frac{1}{2}}_{i+\frac{1}{2},j+\frac{3}{2}} - B^{n+\frac{1}{2}}_{i+\frac{1}{2},j+\frac{1}{2}}\right) + \frac{4\gamma^2}{\alpha\ (\alpha\ + 2)}\left(B^{n+\frac{1}{2}}_{i+\frac{3}{2},j+\frac{1}{2}} - B^{n+\frac{1}{2}}_{i+\frac{1}{2},j+\frac{1}{2}}\right) \tag{29}$$

If in (29) we consider the average value of α, $\bar{\alpha}_{\ ;i+\frac{1}{2},j} = \frac{\alpha_{\ ;i,j} + \alpha_{\ ;i+1,j}}{2}$, one of which is zero for a triangle, we find

$$B^{n+\frac{3}{2}}_{i+\frac{1}{2},j+\frac{1}{2}} - 2B^{n+\frac{1}{2}}_{i+\frac{1}{2},j+\frac{1}{2}} + B^{n-\frac{1}{2}}_{i+\frac{1}{2},j+\frac{1}{2}} = +\frac{\gamma^2}{\bar{\alpha}_\kappa(\bar{\alpha}_\kappa + 1)}\left(B^{n+\frac{1}{2}}_{i+\frac{1}{2},j+\frac{3}{2}} - B^{n+\frac{1}{2}}_{i+\frac{1}{2},j+\frac{1}{2}}\right) + \frac{\gamma^2}{\bar{\alpha}\ (\bar{\alpha}\ + 1)}\left(B^{n+\frac{1}{2}}_{i+\frac{3}{2},j+\frac{1}{2}} - B^{n+\frac{1}{2}}_{i+\frac{1}{2},j+\frac{1}{2}}\right) \tag{30}$$

The two components making up the right hand side of (30) are identical to the right hand side of (8a) with half the magnitude. Therefore, the right hand side of (30) represents two matrices which can be stabilized as in the previous section to have eigenvalues ranging from $[-2, 0]$. Intuitively one would assume the eigenvalues of the sum of these two matrices would have eigenvalues less than, or equal to, the sum of the eigenvalues of each of the matrices (a range of $[-4, 0]$). This hypothesis was tested discretely for all valid values of $0 < (\alpha\ , \alpha_\kappa, \gamma) < 1$ with 0.0025 increments. It was shown the range of eigenvalues of the sum of the matrices was indeed less than or equal to the sum of the eigenvalues of the individual matrices. Therefore, one only has to apply the one-dimensional limiters as defined in the previous section to both components of the **B** update Eq. (27a), and the result is stable.

This analysis holds for triangle cells. In trapezoidal cells, limiting only needs to occur in the direction N_{limit} in Fig. 8 for cell F. If the cell is further enlarged to only cut off one corner of the uncut cell (Fig. 8 cells A and E), no limiting is required.

Special attention is required for the case when the normals of adjacent cells point toward each other in a single dimension (Fig. 8 cells G and H). This case resembles the one-dimensional problem with only two cells, both of which are cut. Applying the limiter (16) at half the magnitude in the direction where the normal reverses stabilizes this special case. This allows for the handling of long, thin cavities. The results of such a test are shown in Fig. 18c in the next section.

Most of the results of the one-dimensional analysis in the previous section still hold true for the two-dimensional case. There is no requirement to reduce the time-step below the CFL limit. The multi-dimensional local truncation error can be computed using the modified equation as was performed in the previous section. This is obtained by substituting the update equation (28) into (18) with the following exact solution for parallel flat plates:

$$B(\ ,\ ) = \mathrm{e}^{\mathrm{i}(\omega\ - k_\parallel \eta)}\cos(k_\perp \zeta) \tag{31}$$

where $k_\parallel$ is the wave number parallel to the boundary and $k_\perp$ is the wave number perpendicular to the boundary, η and ζ are the corresponding coordinates parallel and perpendicular to the boundary. This solution represents a standing wave normal to the boundary and a traveling wave along the boundary. When the

exact solution is substituted into the discrete update equation one ends up with a local truncation error as follows:

$$\tau = \mathrm{O}(1)k_{\parallel} + \mathrm{O}(\Delta) \tag{32}$$

showing that there is an error that is order unity for waves moving along the boundary, but order Δ perpendicular to the boundary. The effects of this will be discussed in more detail in the results section.

As mentioned in the previous section, energy is not strictly conserved. Colella et al. [13] suggest redistributing the non-conserved quantity, energy, to neighboring cells using a volume based weighting. The problem with this approach is that it destroys the divergence free nature of the update, which is maintained by the new scheme. This can be overcome by adding the energy back as a divergence free function, perhaps based on a local projection satisfying the correct boundary conditions and then scaled to replenish (deplete) the lost (gained) energy. In the tests conducted to date, this has not been an issue due to the cancellation effect on incoming and outgoing waves. If this issue becomes problematic, such a solution technique can be employed.

It is important to note that (27b) and (27c) use a non-traditional calculation of the curl operator. Traditionally, the curl is calculated from the loop integral over the control area Ω as follows:

$$\int_{\Omega} \nabla \times \mathbf{B} \cdot \mathrm{d}\Omega = \oint_{\partial\Omega} \mathbf{B} \cdot \mathrm{d}\mathbf{r} \tag{33}$$

Numerically, if one was calculating the discrete curl of $\mathbf{B}$ in the direction one would use the following in three-dimensions:

$$(\nabla \times \mathbf{B} \cdot \hat{\mathbf{n}}_{\mathbf{x}})_{i+\frac{1}{2},j,k} = \frac{B_{;i+\frac{1}{2},j+\frac{1}{2},k}\Delta - B_{\kappa;i+\frac{1}{2},j,k+\frac{1}{2}}\Delta\kappa - B_{;i+\frac{1}{2},j-\frac{1}{2},k}\Delta + B_{\kappa;i+\frac{1}{2},j,k-\frac{1}{2}}\Delta\kappa}{A_{;i+\frac{1}{2},j,k}} \tag{34}$$

However, if one assumes that $A_{;i+\frac{1}{2},j,k} = \Delta\kappa\Delta$ this reduces to the finite-difference form for the curl operator:

$$\frac{B_{;i+\frac{1}{2},j+\frac{1}{2},k} - B_{;i+\frac{1}{2},j-\frac{1}{2},k}}{\Delta\kappa} - \frac{B_{\kappa;i+\frac{1}{2},j,k+\frac{1}{2}} - B_{\kappa;i+\frac{1}{2},j,k-\frac{1}{2}}}{\Delta} \tag{35}$$

On the border of cut cells, we can approximate the $\Delta\kappa$ as follows:

$$\Delta\kappa_{i+\frac{1}{2},j,k} \approx \frac{A_{i+\frac{1}{2},j+\frac{1}{2},k} + A_{i+\frac{1}{2},j-\frac{1}{2},k}}{2\Delta_{\ i+\frac{1}{2},j,k}} \tag{36}$$

This representation of the curl operator, used in (27b) and (27c), reduces to the traditional scheme for uncut cells and represents a difference in $\mathbf{B}$ at points within the cells and is required to ensure stability of the scheme outlined in this document. If one assumes a constant $\mathbf{B}$ within cells adjacent to cut surfaces one can arbitrarily pick points within the cells to be used in differencing for the $\mathbf{E}$ update and still obtain locally first-order accuracy. Therefore, one can maintain a difference normal to the $\mathbf{E}$ edge by adjusting the points accordingly. Fig. 9 shows a stencil near the cut cells, the circles represent the typical differencing points where the diamond points represent the difference points adjacent to a cut cell with the dashed line representing the length used in the difference equation. The choice of location for the points used for differencing is not ideal and actual location of the difference points is not specified. The results presented in the following section validate the accuracy and the stability of the method.

As stated previously, this method satisfies $\nabla \cdot \mathbf{D} = 0$. Matching the operator used for the cut-cell $\mathbf{E}$ update, the divergence is calculated

$$\begin{aligned}\nabla \cdot \mathbf{D} = \frac{4\epsilon}{A_{i+\frac{1}{2},j+\frac{1}{2}} + A_{i+\frac{3}{2},j+\frac{1}{2}} + A_{i+\frac{1}{2},j+\frac{3}{2}} + A_{i+\frac{3}{2},j+\frac{3}{2}}} \Bigg(& E_{i+\frac{3}{2},j+1}\frac{A_{i+\frac{3}{2},j+\frac{1}{2}} + A_{i+\frac{3}{2},j+\frac{3}{2}}}{2\alpha_{i+\frac{3}{2},j+1}h} - E_{i+\frac{1}{2},j+1}\frac{A_{i+\frac{1}{2},j+\frac{1}{2}} + A_{i+\frac{1}{2},j+\frac{3}{2}}}{2\alpha_{i+\frac{1}{2},j+1}h} \\ & + E_{i+1,j+\frac{3}{2}}\frac{A_{i+\frac{1}{2},j+\frac{3}{2}} + A_{i+\frac{3}{2},j+\frac{3}{2}}}{2\alpha_{i+1,j+\frac{3}{2}}h} - E_{i+1,j+\frac{1}{2}}\frac{A_{i+\frac{1}{2},j+\frac{1}{2}} + A_{i+\frac{3}{2},j+\frac{1}{2}}}{2\alpha_{i+1,j+\frac{1}{2}}h}\Bigg)\end{aligned} \tag{37}$$

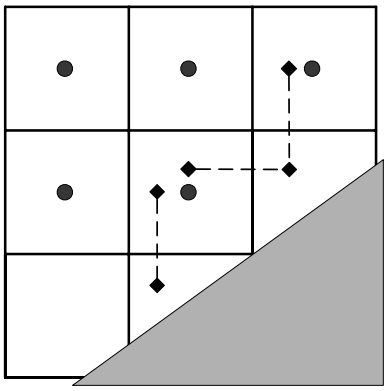

Fig. 9. Illustration of points used in differencing for the magnetic fields. Points represented with circles are for the bulk of the domain, points represented with diamonds are for differences near cut cells, dashed lines represent the lengths used in the differencing.

In regions of uncut cells this reduces to the standard four-point stencil. In regions adjacent to cut cells, (37) represents the finite volume approximation of the divergence with the ratio of area to length representing an approximation of the cross-sectional area.

4.2. Multi-dimensional results

The algorithm was developed and tested for a series of problems, these problems were seeded with an initial B and allowed to oscillate. In cases with exact solutions, the solutions were compared to the exact solution using the multi-dimensional extension of the norms defined in (17).

The first set of tests mimicked what was done in one-dimension. In this example, a square box of length l was rotated $\frac{\Pi}{7}$ radians and seeded with two Gaussian pulses with an initial form of

$$B(\ ,\kappa,\ \ =0)=\mathrm{e}^{100(\ /l-0.5)^2}+\mathrm{e}^{100(\kappa/l-0.5)^2} \tag{38}$$

which was simulated for one oscillation period. The evolving magnetic field should return to the initial condition. Error can be computed by differencing the solution after one oscillation period to the initial solution, thus making $\mathbf{B}_{\text{exact}}=\mathbf{B}_{\text{initial}}$. This test was conducted for three different cases: conformal, non-conformal first-order, and non-conformal modified approach. The results, shown in Fig. 10, show the modified approach

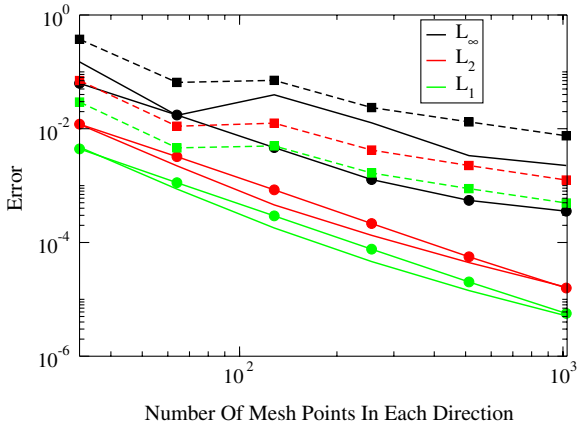

Fig. 10. Error for three configurations of a Gaussian pulse in a square box. Lines with circle symbols represent a fully conformal box, lines with square symbols represent the unmodified Yee's method for a box which has been rotated $\frac{\pi}{7}$ radians. The lines with circle symbols represent the modified algorithm for the same rotation. The errors are displayed for the L_∞, L_1 and L_2 norms with $\gamma=0.89$.

closely following the conformal test for the L_1 and L_2 norms whereas the unmodified Yee's algorithm results in a error which is nearly two orders of magnitude higher.

The modified algorithm was tested with a variety of different CFL conditions ranging from $0.05 < \gamma < 0.9999$ for the same rotated box problem. The resulting error is plotted in Fig. 11. As can be seen, the minimum error for the L_1 and L_2 norms occurs at roughly $\gamma = 0.89$. This is because at that particular point, the flux limiter represents a physical process, not just a numerical convenience. More specifically, at $\gamma = 0.89$ the limiter, α_1, is one half of γ, and therefore, the limiting process exactly represents the reflection of the incoming wave off the conducting surface and back out the incoming face. Thus, the net flux of **B** into a cell is consistent with physics.

The algorithm was also tested on a cylindrical cavity for a TE_{62} mode. The mode was initialized with the analytic **B** field and allowed to oscillate for 10 periods (roughly three transit times for the cavity). The final result was differenced with the initial condition and, as shown in Fig. 12, the convergence follows the second-order convergence curve across six doublings in resolution. The convergence for frequency was computed as well and the results of that are shown in Fig. 13.

In Section 4.1 the local truncation error was estimated to be of order unity for waves traveling parallel to a cut surface, and order Δ for waves perpendicular, and this analysis is borne out by tests of the implementa-

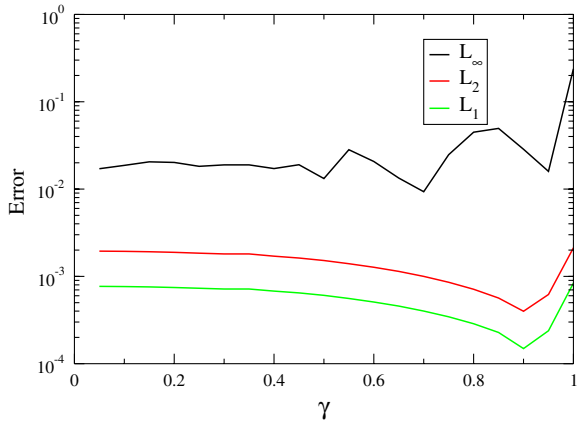

Fig. 11. Error in the L_∞, L_1 and L_2 norms for the modified algorithm on rotated box problem for a 128×128 grid as a function of γ showing an optimal Courant condition of $\gamma = 0.89$.

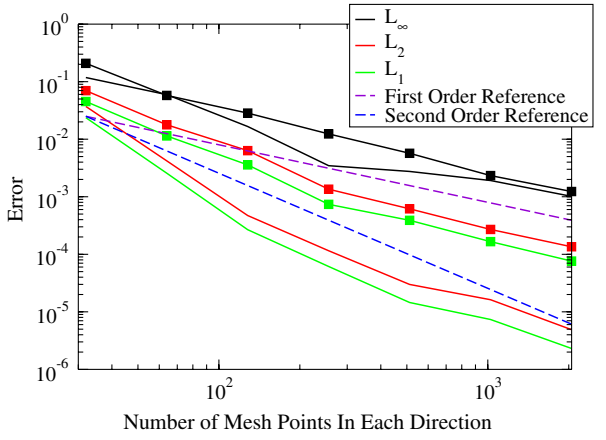

Fig. 12. Convergence for the TE_{62} cavity in the L_∞, L_1 and L_2 norms. Lines without symbols represent the modified algorithm, lines with square symbols represent the unmodified Yee's algorithm.

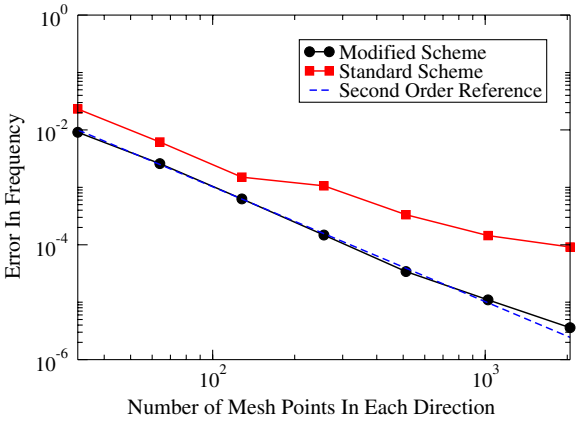

Fig. 13. Convergence for frequency of a TE_{62} in a circular cavity.

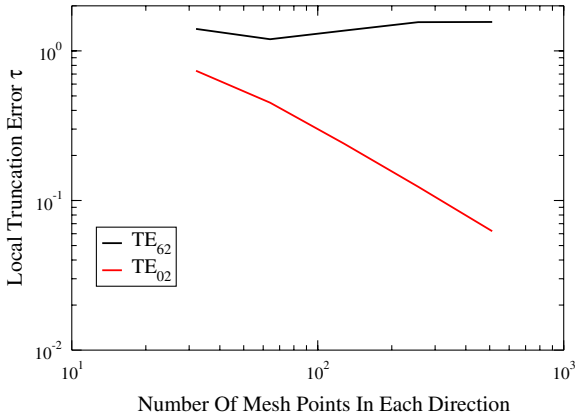

Fig. 14. Local truncation error for two modes (TE_{02} and TE_{62}), for a cylindrical cavity.

tion. The local truncation error was plotted for two different modes in a cylindrical cavity, a TE_{02} and a TE_{62} and is shown in Fig. 14. The axial symmetric TE_{02} mode showed a first-order local truncation error while the TE_{62} mode with a high axial perturbation has a near constant initial error growth.

The constant level of initial local truncation error independent of resolution seems to contradict the results shown previously in Figs. 10 and 12, which show first-order L_∞ convergence. The error tends to grow at a resolution independent rate, and then oscillate with a peak amplitude dependent on the grid resolution and at a frequency much higher then the natural mode of the cavity. This behavior has been seen in several problems and is shown in Fig. 15 for the TE_{62} problem. Furthermore, if one allows the cavity to oscillate long enough it can be seen (Fig. 16) that the order Δ error term dominates causing a linear growth with time in the maximum error in the simulation. These effects yield a long time (greater than a few periods) first-order convergence in the L_∞ norm, and a globally second-order convergence in L_1.

As mentioned earlier, energy is not strictly conserved in the modified algorithm. Discrete energy is computed as follows:

$$W^{n+\frac{1}{2}} = \sum_{i,j=0}^{NX} \frac{\epsilon}{16}\left(E^{n+1}_{;i+\frac{1}{2},j} + E^{n}_{;i+\frac{1}{2},j}\right)^2 \left(A_{i+\frac{1}{2},j-\frac{1}{2}} + A_{i+\frac{1}{2},j+\frac{1}{2}}\right) + \frac{\epsilon}{16}\left(E^{n+1}_{\kappa;i,j+\frac{1}{2}} + E^{n}_{\kappa;i,j+\frac{1}{2}}\right)^2 \left(A_{i-\frac{1}{2},j+\frac{1}{2}} + A_{i+\frac{1}{2},j+\frac{1}{2}}\right) + \frac{\mu}{2}\left(B^{n+\frac{1}{2}}_{i+\frac{1}{2},j+\frac{1}{2}}\right)^2 A_{i+\frac{1}{2},j+\frac{1}{2}} \tag{39}$$

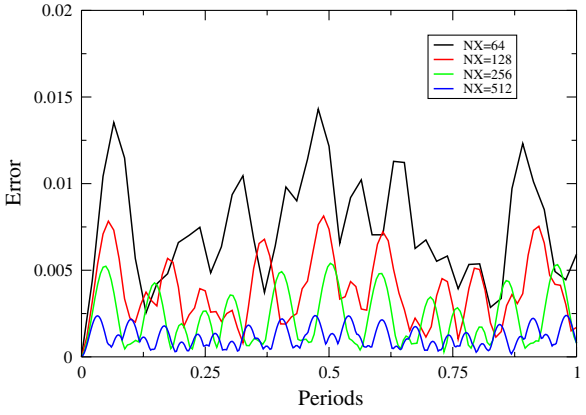

Fig. 15. L_∞ error of a TE_{62} mode in a cylinder over a single period.

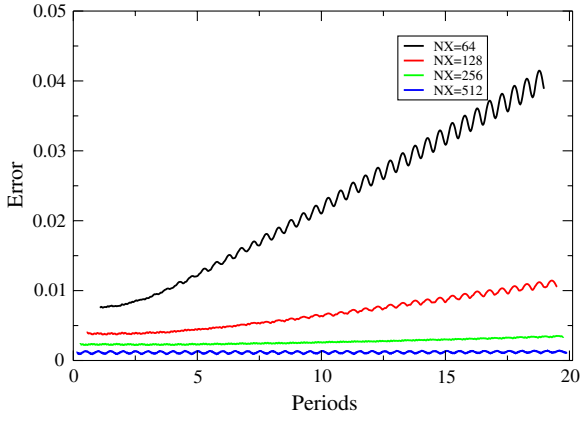

Fig. 16. L_∞ error of a TE_{62} mode in a cylinder over 20 periods. The data has been averages over 100 samples to reduce noise.

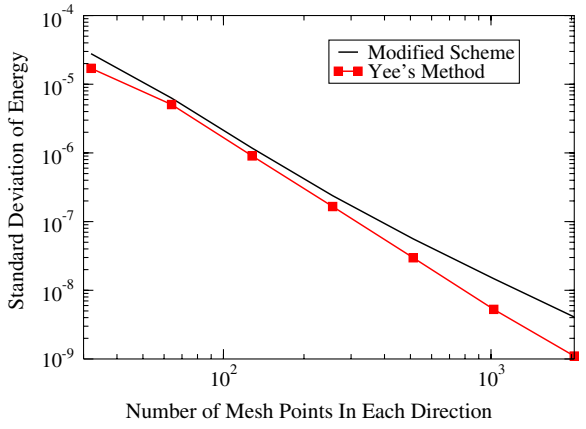

Fig. 17. Standard deviation of energy for the TE_{62} mode problem with a nominal energy of 0.015 J as a function of grid resolution for both Yee's method and the modified scheme.

Neither the standard Yee's method nor the modified scheme is discretely energy conserving due to the temporal averaging in the energy calculation; however, this should converge second-order with grid spacing. Fig. 17 shows the standard deviation of the energy as a function of grid resolution. As can be seen, the modified

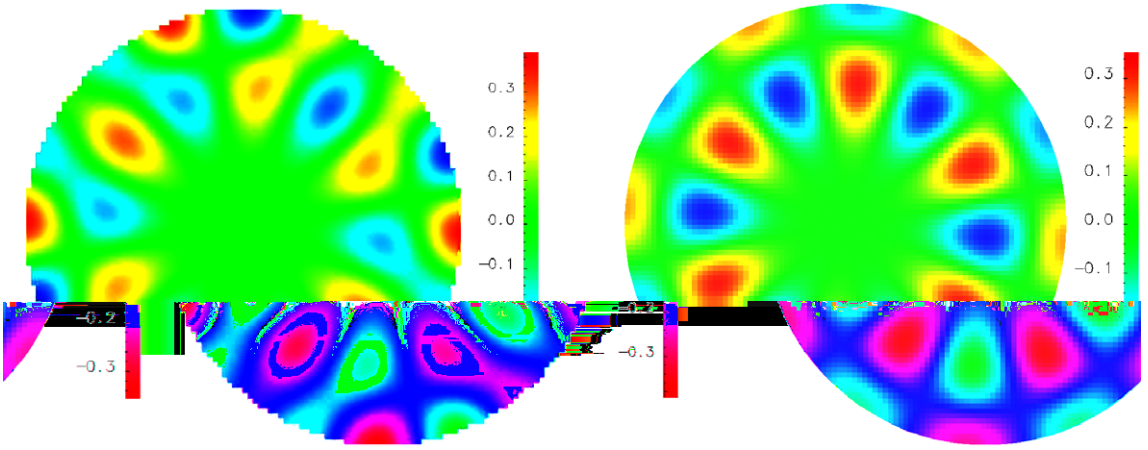

; the (a) TE_{62} mode in circular cavity after 15 oscillations. Grid resolution of 85 cells across diameter.

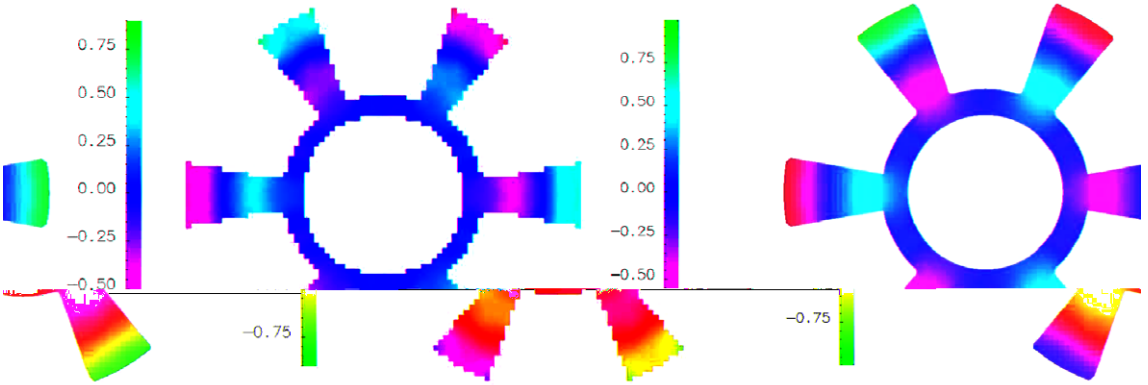

ion of 79 cells across (b) MIT A6 cavity after approximately one transit time. Grid resolut the diameter.

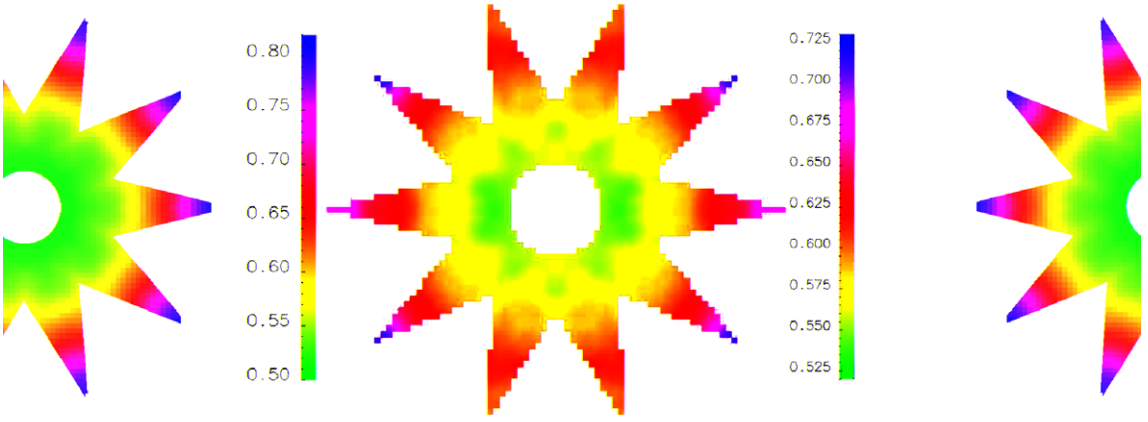

; across the diameter. (c) Star shaped cavity after five transit times. Grid resolution of 81 cells

Fig. 18. Qualitative results for both the standard FDTD algorithm (left) and the modified scheme (right) for several different shapes. The geometry shown in each figure is the computational geometry used for both algorithms with either stair-cased or piece-wise linear boundaries.

scheme has a higher variance in energy, but both curves are converging at equal rates. Simulations were allowed to oscillate for 4000 periods and any growth in average energy was undetectable (not shown).

The scheme was tested on more complicated examples as shown in Fig. 18. These examples are designed to qualitatively test the code for a range of different geometries, all with a degree of radial symmetry. As can be seen in the three examples, there is a much higher degree of symmetry from vane to vane or peak to peak in the modified scheme than with the traditional method. Furthermore, especially for the TE_{62} mode, squaring off and grid alignment of the features is quite prevalent in the traditional FDTD method and is not present in the modified scheme.

Long-time stability is a critical feature for most EM simulations. The three cases shown in Fig. 18 were run for 4000 oscillation periods and their energy averaged over several periods. There is no observed growth in the average energy over hundreds of thousands of time steps.

5. Conclusions and future directions

A uniformly stable algorithm is proposed to handle small geometry in two-dimensions based on a flux limiting scheme. The scheme is shown to require no time-step penalty (however, higher accuracy was shown if the time-step is reduced by roughly 11%), have second-order convergence and to require only a one-dimensional geometric analysis. The scheme is tested for several different physical geometries and shown to produce superior results in all cases. The beauty of the algorithm is in its simplicity. Limiters are based on a mean distance from an edge to a wall, computed as part of a preprocessing step and require no additional work in the update cycle.

The scheme has two areas which cause concern, the first being the initial high truncation error for the scheme. The second is the energy conserving properties of the method. These two areas have not been shown to effect overall accuracy or convergence of the method, however, they should be addressed in the future.

There are two major areas where work is currently underway, or planned to begin shortly. Currently we are attempting to extend this to three-dimensions in a production based code. The algorithm is based on decomposing the multi-dimensional update into a series of one-dimensional updates, each with its own limiter based on a cell averaged one-dimensional geometry. This paradigm can be extended into three-dimensions with one caveat, the flux limiting must be consistent for an edge. For example E affects both B_κ and B, and to maintain the divergence free properties of $\mathbf{B}$, the fluxes must be identical for both B_κ and B. Therefore, the limiter has to be applied consistently to both updates based on the smallest geometric length. In this way one can maintain divergence free solutions.

In conjunction with the extension to three-dimensions, incorporation of particles is a critical effort to be undertaken. The addition of currents to this scheme follows a procedure similar to other FDTD codes. The most important factor is to maintain consistency between the current weighting and the $\mathbf{E}$ update to insure the divergence condition is met. This requires one to scale the current by the local cross-sectional area prior to updating the electric field.

This scheme holds much promise due to the simplicity of the method, the global stability across all CFL values without the requirement of an implicit solve and the superior convergence properties.

References

[1] K.S. Yee, Numerical solution of initial boundary value problems involving Maxwell's equations in isotropic media, IEEE Trans. Antennas Propagat. 14 (1966) 302–307.
[2] K.S. Yee, J.S. Chen, The finite-difference time-domain (FDTD) and the finite-volume time-domain (FVTD) methods in solving Maxwell's equations, IEEE Trans. Antennas Propagat. 45 (3) (1997) 354–363.
[3] K.S. Kunz, K.S. Kunz, R.J. Luebbers, The Finite Difference Time Domain Method for Electromagnetics, CRC Press, 1993.
[4] J.S. Hesthaven, T. Warburton, Nodal high-order methods on unstructured grids, J. Comput. Phys. 181 (2002) 186–221.
[5] K.S. Yee, J.S. Chen, A.H. Chang, Numerical experiments on PEC boundary condition and late timegrowth involving the FDTD/FDTD and FDTD/FVTD hybrid, in: Antennas and Propagation Society International Symposium, 1995, AP-S. Digest, 1, 1995.
[6] G.B. Jacobs, J.S. Hesthaven, High-order nodal discontinuous Galerkin particle-in-cell method on unstructured grids, J. Comput. Phys. 214 (1) (2006) 96–121.
[7] S. Dey, R. Mittra, A locally conformal finite-difference time-domain (FDTD) algorithm for modeling three-dimensional perfectly conducting objects, IEEE Microwave Guided Wave Lett. 7 (9) (1997) 273.

[8] W. Yu, R. Mittra, A conformal FDTD algorithm for modeling perfectly conducting objects with curve-shaped surfaces and edges, Microwave Opt. Technol. Lett. 27 (2) (2000) 136–138.
[9] S. Benkler, M. Chavannes, N. Kuster, A new 3-D conformal PEC FDTD scheme with user-defined geometric precision and derived stability criterion, IEEE Trans. Antennas Propagat. 54 (6) (2006) 1843–1849.
[10] T.G. Jurgens, A. Taflove, K. Umashankar, T.G. Moore, Finite-difference time-domain modeling of curved surfaces [EM scattering], IEEE Trans. Antennas Propagat. 40 (4) (1992) 357–366.
[11] I. Zagorodnov, R. Schuhmann, T. Weiland, A uniformly stable conformal FDTD-method on Cartesian grids, Int. J. Numer. Model 16 (2003) 127–141.
[12] M.J. Berger, R.J. Leveque, Stable boundary conditions for Cartesian grid calculations. Computational technology for flight vehicles, in: Proceedings of the Symposium on Computational Technology on Flight Vehicles, Washington, DC, November 5–7, 1990 (A91-42703 18-59), Comput. Syst. Eng. 1 (2–4) (1990) 305–311, ISSN: 0956-0521.
[13] P. Colella, D.T. Graves, B.J. Keen, D. Modiano, A Cartesian grid embedded boundary method for hyperbolic conservation laws, J. Comput. Phys. 211 (1) (2006) 347–366.
[14] A. Taflove, S.C. Hagness, Computational electrodynamics: the finite-difference time-domain method, Artech House (2000).
[15] P. Colella, Volume of fluid methods for partial differential equations, in: Proceedings of the International Conference on Godunov Methods, October 18–22, 1999, Oxford, UK.